

# Wall-Collision Effect on Optically-Polarized Atoms in Small and Hot Vapor Cells

Yue Chang<sup>1,2,\*</sup> and Jie Qin<sup>1,2</sup>

<sup>1</sup>*Beijing Automation Control Equipment Institute, Beijing 100074, China*

<sup>2</sup>*Quantum Technology R&D Center of China Aerospace Science and Industry Corporation, Beijing 100074, China*

In atomic vapor cells, atoms collide with the inner surface, causing their spin to randomize on the walls. This wall-depolarizing effect is diffusive, and it becomes more pronounced in smaller vapor cells under high temperatures. In this work, we investigate the polarization of optically-pumped alkali-metal atoms in a millimeter-sized cell heated to 150 Celsius. We consider two extreme boundary conditions: fully depolarizing and nondepolarizing boundaries, and we provide an analytical estimation of the polarization difference between them. In the nondepolarizing case, the pump beam's absorption is proportional to the average atomic polarization. However, for fully depolarizing walls, the absorption peak may correspond to a polarization minimum. To mitigate the wall effect, we propose reducing the pump beam's diameter while maintaining the pump power to prevent illumination of the cell wall and increase the pump intensity in the central area. This is crucial for compact vapor-cell devices where the laser frequency can not be detuned since it is locked to the absorption peaks. Additionally, we analyze the wall-depolarizing effect on the performance of an alkali-metal atomic magnetometer operating in the spin-exchange relaxation-free regime. We show that the signal strength is highly limited by wall collisions, and we provide an upper bound for it.

## I. INTRODUCTION

Optically polarized atoms play a crucial role in various fields, including magnetometry [1–3], noble gas hyperpolarization [4–7], atomic clocks [8, 9], quantum optics, and quantum information [10–12], as well as fundamental physics [13–15]. Typically, alkali-metal atoms are confined in a vapor cell and illuminated by a laser beam to transfer the light's polarization to the atoms' spins [16, 17]. However, the atomic polarization can be limited by collisions with the inner cell walls. In particular, the spin of alkali-metal atoms can become almost fully randomized when colliding with the bare glass wall of the cell [18], and this depolarization effect can spread to other parts of the vapor cell through atom-atom collisions. This boundary effect on the overall polarization is more significant in small and hot cells. To mitigate this depolarization effect, antirelaxation coatings with a chemically inert substance such as paraffin can be used. However, paraffin is not stable even at room temperature, and thus, it is not widely used in commercial applications. The development of coatings that can work effectively and remain stable at high temperatures is still a challenge [18–20].

In uncoated vapor cells, ways to mitigate the wall-depolarizing effect include the use of buffer gas, such as nitrogen gas to slow down the motion of atoms by increasing the time spent colliding with the buffer gas, and thus the rate at which they reach the cell wall is reduced [16]. Detuning the pump laser can also reduce the wall effect by decreasing the optical depth and thus the light absorbed by the walls [21]. Most studies on how wall collision affects polarization focus on large (centimeter scale) or low-temperature cells, where the wall effect is

treated as a constant contribution  $\Gamma_{wall}$  to the longitudinal decay rate  $\Gamma_1$ , accounting for the slowest diffusion mode [19, 22]. In this paper, we systematically study the wall-collision effect on small (millimeter scale) and hot (150 Celsius) alkali-metal vapor cells. By numerically solving the diffusion equation [6, 23] with the depolarizing boundary condition, we find that the wall effect may be underestimated when considering only the slowing diffusion mode. We compare the average polarization  $P_{ave}$  in depolarizing-wall cells with that in nondepolarizing-wall cells, obtaining an analytical ratio between these two polarizations as a function of the diffusion constant  $D$ , the longitudinal decay rate  $\Gamma_1$ , the optical pumping rate  $R_{op}$ , and the system size  $L$ . The polarization for depolarizing walls can be much smaller than that with nondepolarizing walls even if  $\Gamma_{wall}$  is added to  $\Gamma_1$  in the nondepolarizing-wall case.

The laser beam's propagation is also considered. We prove that the polarization  $P_{ave}$  in nondepolarizing-wall cells illuminated by uniformly distributed laser beams is independent of the diffusion constant, and it is proportional to the pump laser's absorption. Thus,  $P_{ave}$  can be acquired from the absorption spectrum. However, this relation does not hold for depolarizing boundaries, where an absorption peak may correspond to a local minimum of polarization due to light absorption by the depolarizing wall. We define a quantity,  $\eta_{loss}$ , to characterize the pump beam's loss on the cell walls, which decreases when the pump laser is detuned from the corresponding transition [21]. Reducing the diameter of the laser beam with the same input power also weakens the wall-depolarizing effect on the overall cell, resulting in more polarization achieved with a relatively small input power. This is advantageous to compact vapor-cell based devices where the pump laser's frequency is locked to the absorption peaks.

Finally, we study the wall-depolarization effect on spin-exchange relaxation-free (SERF) magnetometers [24–26],

\* yuechang7@gmail.com

which are one of the most sensitive magnetic-field sensors that typically operate at high temperatures. When integrating an array of these sensors, the spatial distribution of the magnetic field can be detected, requiring a small volume to enhance spatial resolution. By exposing the SERF magnetometer to a small transverse magnetic field, the linear response  $P_x$  is extracted. If the atoms are homogeneously polarized, the transverse signal  $P_x$  is maximum when the longitudinal polarization  $P_{ave}$  is  $1/2$  [19]. However, including diffusion, the largest  $P_x$  occurs at a smaller  $P_{ave} < 1/2$  for depolarizing boundaries. Moreover, when the wall is perfectly coated to prevent depolarization, the signal  $P_x$  can increase by an order of magnitude, even with the depolarizing-wall cell filled with thousands of Torr of nitrogen gas. We provide an upper bound of the optimal  $P_x$  for the depolarizing-wall case, which facilitates efficient signal magnitude estimation without having to solve diffusion equations for atomic spins and Maxwell equations for light propagation. We also find that reducing the illuminated area can enhance the transverse signal  $P_x$ .

The organization of this paper is as follows. In Section II, we begin by examining the case where the vapor cell is uniformly illuminated. Using  $^{87}\text{Rb}$  as an example, we solve the atomic diffusion equation and the light-propagation equation under two extreme boundary conditions: fully depolarizing and nondepolarizing walls. We present the distribution of the polarization and the light intensity in a cylindrical cell, as well as an analysis of the average polarization and the light transmission. Additionally, we define the portion  $\eta_{loss}$  of light absorbed by the cell walls. In Section III, we investigate the transverse signal  $P_x$  of a SERF magnetometer under various physical conditions and analyze the optimal  $P_x$ . Moving on to a partially illuminated vapor cell, Section IV examines the dependence of the polarization  $P_{ave}$ , the light transmission, and the performance of SERF magnetometers on the diameter of the laser beam. Finally, in Section V, we summarize our work.

## II. ATOMIC POLARIZATION AND LIGHT TRANSMISSION

In this section, we will solve the light propagation equation along with the atomic diffusion equation and obtain the light transmission and the atom's polarization. Without loss of generality, we assume that the vapor cell is cylindrical with a length of  $L$  and a radius of  $R$ , as shown in Fig. 1. The pump beam propagates in the  $z$  direction and has a cross-section radius of  $r_L$ . The longitudinal axis of the cylindrical cell is the same as the laser beam's, so the system has cylindrical symmetry. Therefore, the polarization and light intensity  $I$  within the cell are functions of the longitudinal coordinate  $z \in [0, L]$  and radial distance  $r \in [0, R]$ . In the high-temperature limit, the atomic state can be well approximated by the spin-temperature distribution [6, 24]

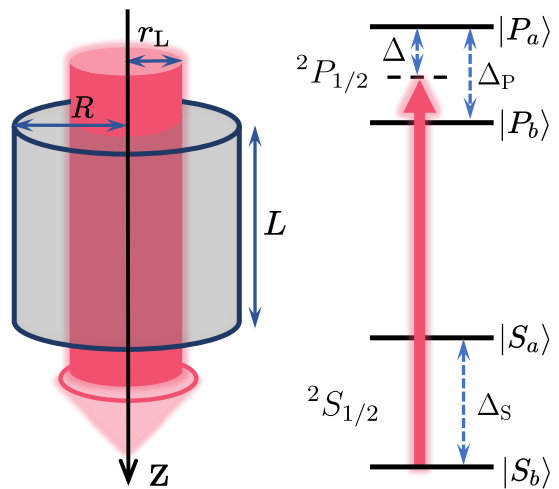


FIG. 1. Schematic of a cylindrical vapor cell (grey cylinder) optically pumped by a laser beam (red beam) with a radius of  $r_L$ . The cell has a longitudinal length of  $L$  and a radius of  $R$  and is filled with alkali-metal atoms and buffer gas. The energy level of the alkali-metal atom is shown on the right. The pump laser couples to the ground states  $^2S_{1/2}$  and the first excited states  $^2P_{1/2}$  (D1 transition) with a detuning of  $\Delta$ . Due to the hyperfine interaction, the ground (excited) states are split into two manifolds  $|S_a\rangle$  and  $|S_b\rangle$  ( $|P_a\rangle$  and  $|P_b\rangle$ ), respectively, with an energy difference of  $\Delta_S$  ( $\Delta_P$ ).

and we can characterize the atomic polarization  $\langle F_z \rangle$  by the electronic polarization  $P_e \equiv 2 \langle S_z \rangle$  and the slow-down factor  $q(P_e) \equiv \langle F_z \rangle / \langle S_z \rangle$  is a function of  $P_e$ . Here,  $F_z$  ( $S_z$ ) is the total (electronic) spin in the  $z$  direction. After eliminating adiabatically the excited states [27],  $P_e(z, r)$  in the steady state satisfies the following equation

$$D\nabla^2 q(P_e) P_e - (R_{op} + \Gamma_{rel}) P_e + R_{op} = 0, \quad (1)$$

where  $D$  is the diffusion constant,  $\Gamma_{rel}$  is the atom-collision induced spin-destruction rate, and  $R_{op} = g_P \mathcal{L}(\Delta) I$  is the optical pumping rate. Here,  $g_P$  is the square of the dipole moment  $\langle d \rangle$  and  $\mathcal{L}(\Delta)$  the lineshape, which will be explicitly given later. Note that we assume the collisions are strong enough so that the atoms are in a local spin-temperature distribution with the spin temperature varying as a function of the atom's coordinate  $(z, r)$ . Additionally, we fill the cell with a buffer gas, such as nitrogen gas to weaken the wall effect and suppress radiation trapping [28]. This ensures that photons emitted from atomic excited states are mostly absorbed by  $N_2$ , making it possible to neglect the reflection of the laser beam. Consequently, we can linearize the forward propagation equation of light as follows:

$$\partial_z I = -g_I \mathcal{L}(\Delta) I (1 - P_e). \quad (2)$$

Here,  $g_I = n_A k \langle d \rangle^2$ , where  $n_A$  is the density of alkali atoms and  $k$  is the laser's wavenumber.

For  $^{87}\text{Rb}$ , the slow-down factor

$$q(P_e) = \frac{6 + 2P_e^2}{1 + P_e^2} \quad (3)$$

and the lineshape can be described as a sum of four Lorentzian functions corresponding to four transitions between two ground-state and two excited-state manifolds. This is given by

$$\mathcal{L}(\Delta) = \frac{\Gamma_L}{16\pi} \left[ \frac{5}{\Delta^2 + \Gamma_L^2} + \frac{5}{(\Delta - \Delta_S - \Delta_P)^2 + \Gamma_L^2} + \frac{5}{(\Delta - \Delta_S)^2 + \Gamma_L^2} + \frac{1}{(\Delta - \Delta_P)^2 + \Gamma_L^2} \right], \quad (4)$$

where  $\Gamma_L$  is the decay rate of the excited states and is proportional to the density of nitrogen gas. We consider the conditions:  $150^\circ\text{C}$ ,  $200\text{Torr } N_2$ ,  $L = 2R = 2\text{mm}$ , and  $\Delta = 0$ , and plot the polarization  $P_e(z, r)$  and normalized light intensity  $I(z, r)/I_0$  in Fig. 2. Here,  $I_0 \equiv I(0, 0)$  represents the laser intensity at the incident plane, and the input laser power is  $0.5\text{mW}$ , illuminating uniformly on the entire cell ( $r_L = R$ ). For depolarizing walls, the polarization  $P_e^{De}(z, r)$  (Fig. 2(a)) is maximum at the center  $r = 0$  and decays towards the boundaries due to depolarization of the walls and decrease in light density. The decrease in light intensity is shown in Fig. 2(b), where the intensity  $I^{De}(z, r)$  monotonically decreases along the propagation direction and decays from the center to the boundaries. To illustrate this explicitly, Figs. 2(c) and 2(d) show the decay of  $I^{De}(z, r)$  along the radial and longitudinal directions, respectively. For comparison, we show  $P_e^{NonDe}(z, r)$  and  $I^{NonDe}(z, r)/I_0$  for nondepolarizing walls in Figs. 2(e) and 2(f), respectively. Here,  $P_e^{NonDe}(z, r)$  and  $I^{NonDe}(z, r)$  change only along the pump laser's propagation direction, and the atomic spins are nearly fully polarized ( $\sim 0.99$ ), leading to a close-to-unity  $I^{NonDe}(z, r)/I_0$ .

By integrating Eqs. (1) and (2) we obtain

$$1 - T = \frac{gI}{I_{in}gP} \left[ V\Gamma_{rel}P_{ave} - D \oint d\mathbf{S} \cdot \nabla (q(P_e) P_e) \right], \quad (5)$$

where

$$T = \frac{\int_{z=L} dS I(r, L)}{I_{in}}, \quad (6)$$

represents the transmission probability,  $S$  is the cell wall,

$$I_{in} = \int_{z=0} dS I(r, 0), \quad (7)$$

depicts the total input power, while  $P_{ave}$  is the average polarization over the cell volume  $V$ :

$$P_{ave} = \frac{1}{V} \int_V dV P_e. \quad (8)$$

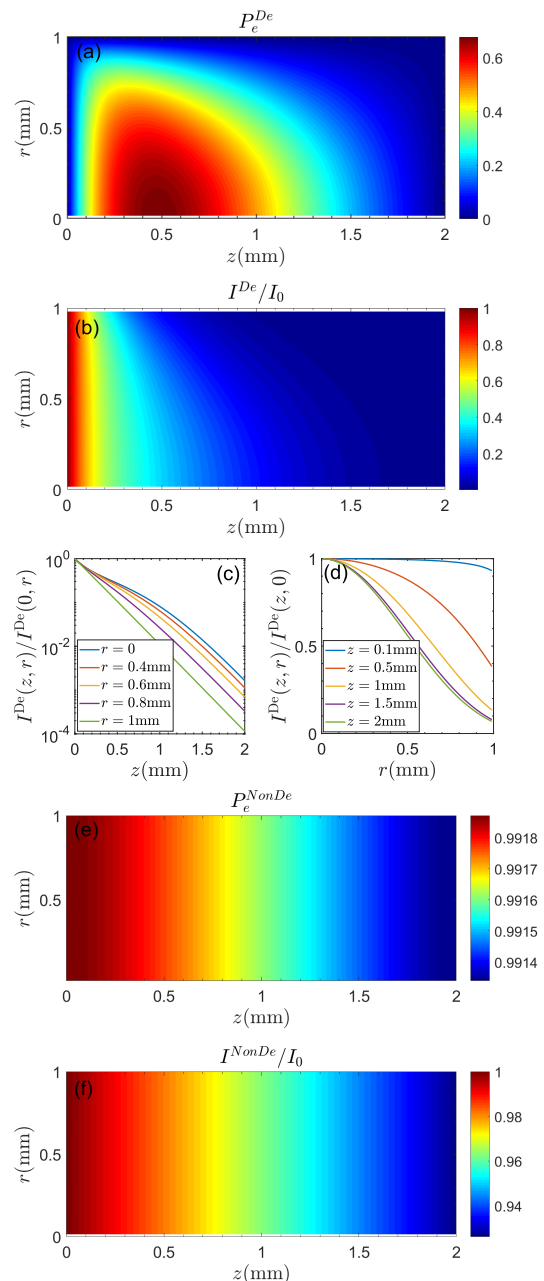


FIG. 2. Polarization  $P_e(z, r)$  and light intensity  $I(z, r)$  distributions within the vapor cell for depolarizing (a)-(d) and nondepolarizing (e)-(f) boundaries.

If the wall does not depolarize spins ( $\nabla P_e|_S = 0$ ), we obtain a simplified expression:

$$1 - T = \frac{V\Gamma_{rel}gI}{I_{in}gP} P_{ave} \quad (9)$$

since  $\nabla (q(P_e) P_e) = \partial_{P_e} (q(P_e) P_e) \nabla P_e$ . This implies that the absorbed light is entirely transferred to the spin polarization  $P_{ave}$  and that they have a one-to-one correspondence. Additionally, it can be proved (see Appendix A) that the absorption/polarization peak occurs

at  $\partial_{\Delta}\mathcal{L}(\Delta) = 0$ .

In the case of depolarizing walls,  $P_e|_S = 0$  and the relation (9) no longer holds. At the cell walls,  $\nabla(q(P_e)P_e)$  is negative in the direction of  $d\mathbf{S}$  ( $\partial_{P_e}(q(P_e)P_e) = 2\partial_{P_e}\langle F_z \rangle > 0$ ), and  $\oint d\mathbf{S}\cdot\nabla(q(P_e)P_e) < 0$ . Consequently, more light is absorbed for depolarizing boundaries, but some of it does not transfer to the spin polarization and is lost in the cell walls. To quantify this loss, we define the portion of light lost  $\eta_{loss}$  as follows:

$$\eta_{loss} = 1 - T - \frac{V\Gamma_{rel}g_I}{I_{in}g_P}P_{ave}. \quad (10)$$

For different  $N_2$  pressures and input powers, we show the average polarization  $P_{ave}^{De}$ , the transmission probability  $T$ , and the loss  $\eta_{loss}$  in Fig. 3. For small gas pressures (200Torr) and input powers ( $< 3\text{mW}$ ), the transmission  $T$  has two minima at  $\Delta \approx 0$  and  $\Delta \approx \Delta_S$ , respectively (the energy splitting in the excited states can not be distinguished because  $\Gamma_L \sim \Delta_P$ ), while the polarization  $P_{ave}^{De}$  is minimal at these two absorption peaks (Figs. 3(a)). This is due to the large loss of light on the walls, as shown in Figs. 3(b), where the absorption of light by the wall is maximal at the resonant points 0 and  $\Delta_S$  since the bare absorption length  $\lambda_L \equiv [g_I\mathcal{L}(\Delta)]^{-1}$  of the laser is shortest (assuming the polarization is zero). This is also true for larger input powers. When the laser power increases to 3mW, the wall-depolarizing effect is reduced since  $P_{ave}^{De}$  is larger, so the absorption-polarization relation is closer to the nondepolarizing-wall case and the absorption peaks correspond to polarization peaks. Furthermore, decreasing the diffusion constant  $D$  by increasing the  $N_2$  pressure can also reduce the wall-depolarizing effect. In Figs. 3(c) and (d), when the nitrogen gas pressure is increased from 200Torr to 500Torr and 1000Torr, the two absorption peaks, as well as the two peaks in the loss  $\eta_{loss}$  merge into one peak since  $\Gamma_L \sim \Delta_S$ , where the polarization is maximal. With larger  $N_2$  pressures,  $P_{ave}^{De}$  and  $T$  become larger, because the wall-depolarizing effect is smaller (Fig. 3(d)) and meanwhile, the absorption length  $\lambda_L$  is larger.

For comparison, the polarization and transmission for nondepolarizing walls are illustrated in Fig. 4. As proved in Appendix A, there exist absorption/polarization peaks at  $\partial_{\Delta}\mathcal{L}(\Delta) = 0$ . For low gas pressure (200Torr), the polarization  $P_{ave}^{NonDe}$  exhibits two peaks at  $\Delta \approx 0$  and  $\Delta \approx \Delta_S$ , corresponding to two transmission minima (Fig. 4(a)). With increasing  $N_2$  pressure, the two peaks become indistinguishable, and both the polarization  $P_{ave}^{NonDe}$  and the transmission  $T$  decrease (Fig. 4(c)). The decrease in transmission is due to the increase in  $\Gamma_{rel}$ , which exceeds the effect of  $\lambda_L$ 's increment on the polarization. In the absence of depolarization on the walls, the transmission  $T$  is close to unity and the polarization  $P_{ave}^{NonDe}$  is much larger than  $P_{ave}^{De}$ . Therefore, the ratio  $P_{ave}^{De}/P_{ave}^{NonDe}$  can also be used to characterize the wall-depolarization effect, as plotted in Figs. 4(b) and (d) in blue lines. Like the light lost  $\eta_{loss}$ , the ratio  $P_{ave}^{De}/P_{ave}^{NonDe}$  can be increased by detuning the pump

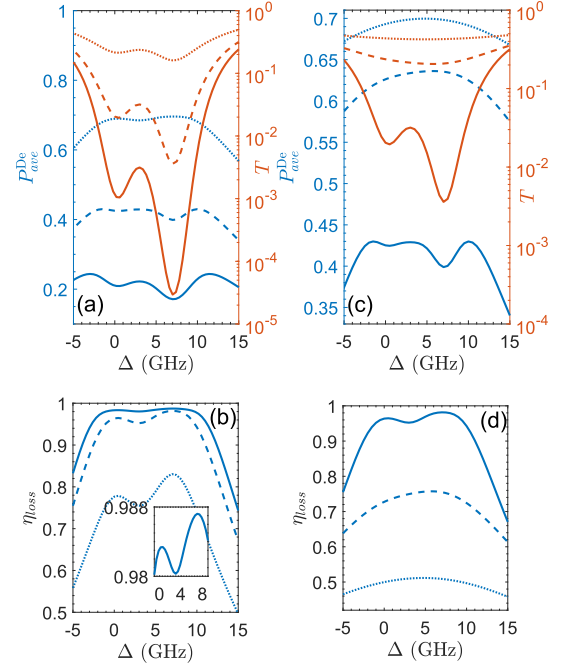


FIG. 3. Average polarization  $P_{ave}$  (blue lines in (a) and (c)), transmission probability  $T$  (red lines in (a) and (c)), and the ratio  $\eta_{loss}$ , representing the fraction of pump absorbed by the cell walls ((b) and (d)) for depolarizing walls. In (a) and (b), the  $N_2$  pressure is 200Torr, and the input powers are 0.5mW (solid lines), 1mW (dash lines), and 3mW (dotted lines). In contrast, in (c) and (d), the input power is fixed at 1mW, while the  $N_2$  pressures are varied from 200Torr (solid lines), to 500Torr (dash lines) and 1000Torr (dotted lines). The inset in (b) explicitly shows the two absorption peaks of the light by the depolarizing walls. All other parameters are identical to those in Fig. 2.

laser, increasing the pump power, or increasing  $N_2$  density. Apart from solving the nonlinear equations (1) and (2), this ratio  $P_{ave}^{De}/P_{ave}^{NonDe}$  can also be estimated as (see Appendix B for the derivation)

$$\frac{P_{ave}^{De}}{P_{ave}^{NonDe}} \approx \sqrt{1 - \frac{\lambda_D}{\lambda_L}} \left(1 - 2\frac{\lambda_D}{L}\right) \left(1 - \frac{\lambda_D}{R}\right)^2 \quad (11)$$

where

$$\lambda_D = \sqrt{\frac{qD}{\Gamma_{rel} + R_{op}^0}}. \quad (12)$$

Here,  $\lambda_D$  is the wall-depolarization length with  $R_{op}^0 \equiv g_P\mathcal{L}(\Delta)I_0$ . The validity of this estimation requires the ratio  $\lambda_D/\lambda_L$  between the wall-depolarization length  $\lambda_D$  and the absorption length  $\lambda_L$  is smaller than 1. The smaller  $\lambda_D/\lambda_L$ , the better the analytical estimation, as shown in Figs. 4(b) and (d) in red lines. The ratio  $\lambda_D/\lambda_L$  can be reduced by increasing the incident light density  $I_0$  or the detuning  $\Delta$  from the resonant points,

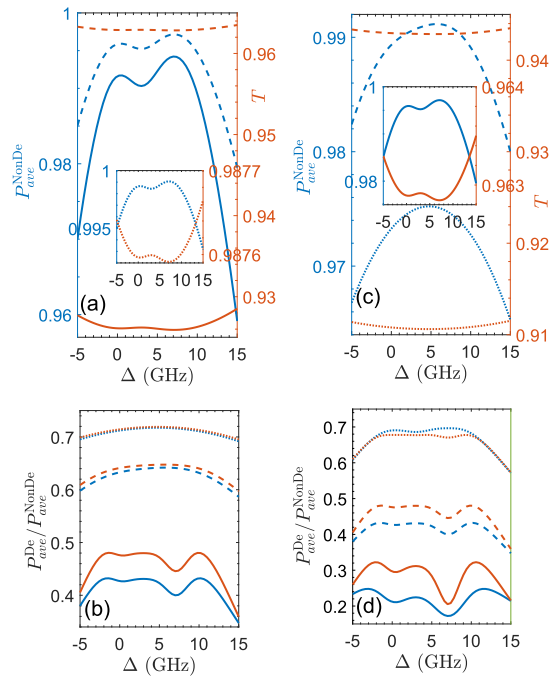


FIG. 4. Average polarization  $P_{ave}^{NonDe}$  (blue lines in (a) and (c)) and transmission probability  $T$  (red lines in (a) and (c)) for nondepolarizing walls. The ratio  $P_{ave}^{De}/P_{ave}^{NonDe}$  is shown in (b) and (d). Similar to Figs. 3, the  $N_2$  pressure is fixed at 200 Torr in (a) and (b), while input powers of 0.5 mW (solid lines), 1 mW (dash lines), and 3 mW (dotted lines) are used. In (c) and (d), the input power is fixed at 1 mW, and  $N_2$  pressures of 200 Torr (solid lines), 500 Torr (dash lines), and 1000 Torr (dotted lines) are used. The remaining parameters are identical to those in Fig. 2. The numerical results are shown with blue lines in (b) and (d), while the analytical estimation using Eq. (11) is shown with red lines. In this case, the slow-down factor  $q$  in Eq. (11) is fixed at 5.

or decreasing the diffusion constant  $D$ . When  $\lambda_D/\lambda_L$  is not sufficiently small so that the approximation (11) is not perfect (solid lines in Figs. 4(b) and (d)), but it still provides an upper bound for  $P_{ave}^{De}/P_{ave}^{NonDe}$ , since we have assumed the light density  $I$  does not change much within the wall-depolarization length and  $\lambda_D$  consequently depends solely on the initial value  $I_0$ . Note that the slow-down factor  $q$  is a function of the local polarization  $P_e(z, r)$  but a median value can be used to simplify the calculation. For  $^{87}\text{Rb}$ ,  $q$  varies between 4 (fully polarized) and 6 (zero polarization), and we take  $q = 5$  in Eq. (11).

Literally, a commonly used approach to account for the depolarizing-wall effect is to introduce a spin-depolarization rate  $\Gamma_{wall}$ , which is determined by the lowest diffusion mode, to the longitudinal relaxation rate. In this study, we investigate this method by substituting  $\tilde{\Gamma}_{rel} = \Gamma_{rel} + \Gamma_{wall}$  for the nondepolarizing-wall case. For

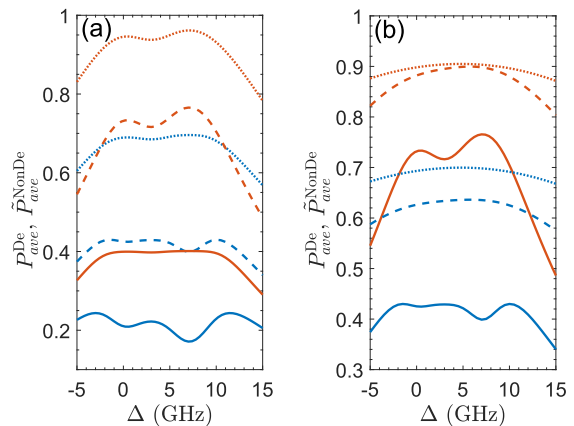


FIG. 5. Average polarization  $\tilde{P}_{ave}^{NonDe}$  (red lines) for nondepolarizing walls by including  $\Gamma_{wall}$  (with slow-down factor  $q = 6$ ) in the longitudinal decay. In comparison,  $P_{ave}^{De}$  is shown in blue lines. Similar to Figs. 3, (a) displays the results for  $N_2$  pressure of 200 Torr and input powers of 0.5 mW (solid lines), 1 mW (dashed lines), and 3 mW (dotted lines). In (b), the input power is constant at 1 mW, while the  $N_2$  pressures vary among 200 Torr (solid lines), 500 Torr (dash lines), and 1000 Torr (dotted lines). All other parameters remain unchanged from Fig. 2.

cylindrical cells,

$$\Gamma_{wall} = qD \left[ \left( \frac{\pi}{L} \right)^2 + \left( \frac{\mu_1}{R} \right)^2 \right], \quad (13)$$

where  $\mu_1$  is the first zero of the Bessel function of the first kind [21, 29]. By taking the maximum value of  $q = 6$  in Equation (13), we depict  $\tilde{P}_{ave}^{NonDe}$  in Figure 5 with red lines, while  $P_{ave}^{De}$  is shown with blue lines for comparison. Our findings reveal that, even with the inclusion of  $\Gamma_{wall}$  in  $\Gamma_{rel}$ , the polarization  $\tilde{P}_{ave}^{NonDe}$  can be significantly larger than  $P_{ave}^{De}$ . Thus, this simplistic approach may underestimate the wall-depolarizing effect.

### III. WALL EFFECT ON SERF MAGNETOMETERS

In this section, we take SERF magnetometers [1, 24, 25] as an example to study the wall effect on the transverse signals  $P_x \equiv 2 \langle S_x \rangle$ . SERF magnetometers are highly sensitive to magnetic fields and do not suffer from spin-exchange relaxation, which is a major source of spin-decoherence in atomic magnetometers. In order to operate in the SERF regime, SERF magnetometers are typically used at high temperatures and low magnetic fields  $B$ . Here, we assume the magnetic field  $B$  to be along the  $y$  direction, and its induced energy splitting much smaller than the spin-destruction rate  $\Gamma_{rel}$ . As in Sec. II, we assume that the atomic system is approximately in a spin-temperature distribution. To the first order of the small magnetic field  $B$ ,  $P_x$  in the long-term limit



satisfies the following equation

$$D\nabla^2 q(P_e) P_x - (R_{op} + \Gamma_{rel}) P_x + \gamma_e B P_e = 0, \quad (14)$$

where  $\gamma_e$  is the electron's gyromagnetic ratio and  $\gamma_e B \ll \Gamma_{rel}$ . Note that here, we have ignored the light shift induced by the pump laser, as it is usually compensated for by a magnetic field along the  $z$  direction in practical use.

The solution  $P_x^{De}(z, r)$  to Eq. (14) for depolarizing boundaries is depicted in Fig. 6(a), where the parameters used are the same as in Fig. 2(a). It can be observed that Fig. 6(a),  $P_x^{De}(z, r)$  reaches its maximal value in the region where  $P_e^{De}(z, r) \approx 1/2$ , which is consistent with the simple model of SERF magnetometers that disregards the light propagation and atomic diffusion. However, it should be noted that the maximum of the total transverse signal

$$P_{x,ave} \equiv \frac{1}{V} \int_V dV P_x \quad (15)$$

appears at  $P_{ave}^{De} < 1/2$  (See Figs.6(b) and (c)). This is because the polarizations  $P_e^{De}(z, r)$  decays as it approaches the cell walls. For small  $P_{ave}^{De}$  (solid lines in Fig.6(b) and (c)), the transverse signal  $P_{x,ave}$  locally reaches its minimum at the absorption peaks, where  $P_{ave}^{De}$  is also locally minimal. This behavior preserves even for large input region, as depicted by the dash and dotted lines in 6(b) and (c). This is in contrast to  $P_{ave}^{De}$ , since with large input power,  $P_{ave}^{De}$  reaches a local maximum and exceeds  $1/2$  at the absorption peaks.

To increase the total transverse signal  $P_{x,ave}$ , one can enlarge the region where the electron polarization  $P_e^{De}(z, r)$  is approximately  $1/2$ , since the transverse polarization  $P_x^{De}(z, r)$  is large in this region. This can be achieved by increasing the buffer gas density or by detuning the pump laser while increasing its power to compensate for the decrease in optical pumping rate. Optimal signals  $\tilde{P}_{x,ave}^{De}$  are obtained for different input powers of the pump laser by varying the detuning  $\Delta$  for different  $N_2$  pressures. As shown in Figure 7(a), for a given  $N_2$  pressure, the maximal signal  $\tilde{P}_{x,ave}^{De}$  saturates as the input power increases because the wall-depolarization length  $\lambda_D$  saturates and the region where  $P_e^{De}(z, r) \approx 1/2$  does not extend. With more  $N_2$ , the wall-depolarization length  $\lambda_D$  saturates at a smaller value and the region where  $P_e^{De}(z, r) \approx 1/2$  is further enlarged, resulting in a larger  $\tilde{P}_{x,ave}^{De}$  ( $\tilde{P}_{x,ave}^{De}|_{500\text{Torr}} < \tilde{P}_{x,ave}^{De}|_{1000\text{Torr}} < \tilde{P}_{x,ave}^{De}|_{2000\text{Torr}}$ ). However, the dependence of  $\tilde{P}_{x,ave}^{De}$  on the  $N_2$  pressure is not monotonic, because  $P_x^{De} = \gamma_e B P_e^{De} / (R_{op} + \Gamma_{rel})$  when ignoring the spatial dependence and  $\Gamma_{rel}$  is larger with more buffer gas. Therefore,  $\tilde{P}_{x,ave}^{De}|_{3000\text{Torr}} < \tilde{P}_{x,ave}^{De}|_{2000\text{Torr}}$  since the increase in  $\Gamma_{rel}$  has a greater influence than the suppression of the wall-depolarization effect.

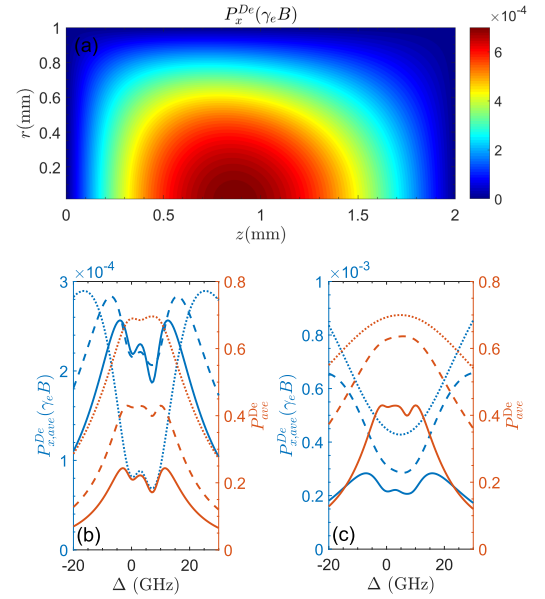


FIG. 6. The spatial dependence of  $P_x^{De}(z, r)$  for depolarizing walls is displayed in (a), using the same parameters as in 2(a). In (b) and (c), the average signal  $P_{x,ave}$  is represented by blue lines, while the corresponding polarization  $P_{ave}^{De}$  is depicted by red lines. Same as in Fig. 3, the  $N_2$  pressure is 200Torr and the input powers are 0.5mW (solid lines), 1mW (dashed lines), and 3mW (dotted lines) in (b). In (c), the input power is 1mW, and the  $N_2$  pressures are 200Torr (solid lines), 500Torr (dashed lines), and 1000Torr (dotted lines). All other parameters remain the same as in Fig. 2.

The optimal transverse signal  $\tilde{P}_{x,ave}^{De}$  for depolarizing walls can be estimated analytically as (see Appendix B for details)

$$\tilde{P}_{x,ave}^{De} \approx \min\{r_1, r_2\}, \quad (16)$$

where

$$r_1 = \max \left[ \frac{P_{ave}^{De}}{P_{ave}^{NonDe}} \frac{\gamma_e B R_{op}^0}{(R_{op}^0 + \Gamma_{rel})^2} \right]$$

and

$$r_2 = \max \left[ \frac{P_{ave}^{De}}{P_{ave}^{NonDe}} \frac{\gamma_e B}{2(R_{op}^0 + \Gamma_{rel})} \right]. \quad (17)$$

This analytical upper bound of  $\tilde{P}_{x,ave}^{De}$  is shown in Fig. 7(a), which has up to 30% deviation from the exact numerical values. Therefore, using the simple expression in Eq. (16) can be helpful to determine the optimal parameters without solving the nonlinear equations. It should be noted that even with optimized parameters, the transverse signal for depolarizing walls can be significantly smaller than the non-depolarizing wall case. For

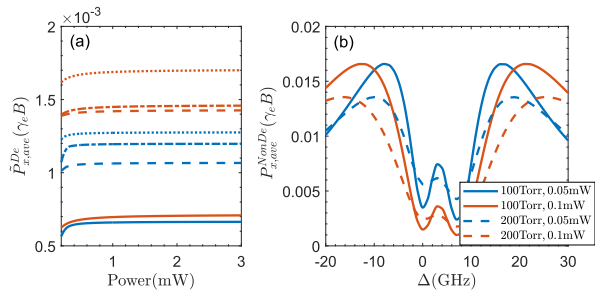


FIG. 7. (a) Transverse signal  $\tilde{P}_{x,ave}^{De}$  as a function of the pump laser power at various  $N_2$  pressures. The blue lines represent the numerical results obtained by varying the detuning  $\Delta$ , while the red lines represent the analytical estimation (Eq. (16)) that provides an upper bound for  $\tilde{P}_{x,ave}^{De}$  with a difference of no more than 30%. The  $N_2$  pressures considered are 500 Torr (solid lines), 1000 Torr (dashed lines), 2000 Torr (dotted lines), and 3000 Torr (dash-dotted lines). The remaining parameters are the same as in Fig. 2(a). (b) Transverse signal  $P_{x,ave}^{NonDe}$  for nondepolarizing walls at a temperature of 150 Celsius.

example, for 100Torr and 200Torr  $N_2$ , which are sufficient to suppress radiation trapping, the latter case is presented in Fig. 7(b). In this case, the signal  $P_{x,ave}^{NonDe}$  can be one order of magnitude larger than  $\tilde{P}_{x,ave}^{De}$  due to the strong wall-depolarizing effect in small vapor cells.

#### IV. PARTIALLY ILLUMINATED CELLS

Uncoated cells exhibit depolarization of atoms in the vicinity of the boundary, within a distance of  $\lambda_D$ . To mitigate this wall-depolarizing effect, the laser beam can be concentrated on the central region of the cell while maintaining constant input power or  $I_{in}$ . To demonstrate this, we simulate the atomic polarization  $P_e^{De}(z, r)$  and the light intensity  $I^{De}(z, r)/I_0$ , with a laser radius of 0.8mm and input power of 0.5mW, depicted in Figs. 8(a) and (b), respectively. While the light is confined to the central region of the cell due to radial non-propagation, the atomic polarization in the un-illuminated region is still non-zero as spins diffuse in all directions via collisions. Note that the incident light intensity  $I_0$  is dependent on the illumination area as  $I_0 = I_{in}/(\pi r_L^2)$ . Our results show that the partially illuminated cell exhibits more centralized atomic polarization and a slower rate of decay of the light intensity  $I^{De}(z, r)/I_0$  along the  $z$ -direction, as compared to Figs. 2(a) and (b). The overall effect is depicted in Figs. 8(c) and (d), where the average polarization  $P_{ave}^{De}$  and light transmission  $T$  are both increased, resulting in a reduced light loss  $\eta_{loss}$  due to the wall.

The impact of centralizing the laser beam on the wall-depolarizing effect is most evident at resonant points that correspond to absorption peaks. This is highly beneficial for compact atomic-vapor-cell based devices, the fre-

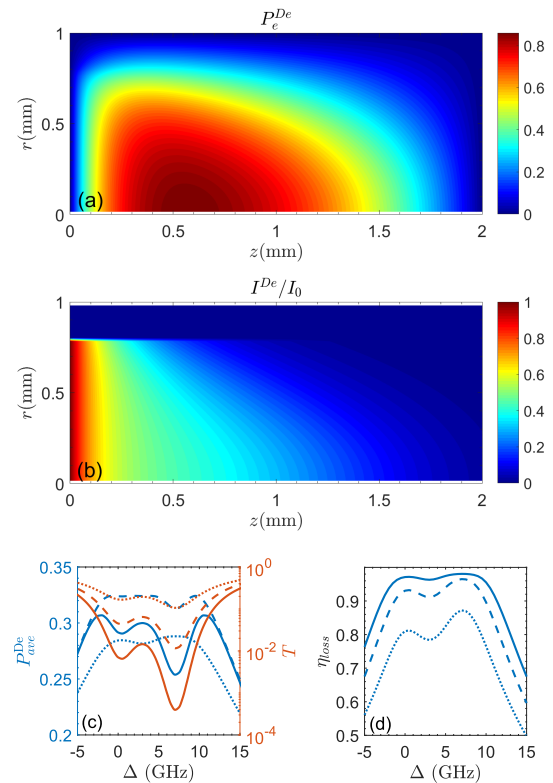


FIG. 8. Spatially dependent atomic polarization  $P_e^{De}(z, r)$  (a) and normalized light intensity  $I^{De}(z, r)/I_0$  (b) for partially illuminated, uncoated cells with laser beam radius  $r_L = 0.8\text{mm}$ , while the other parameters are kept the same as in Fig. 2(a). The average polarization  $P_{ave}^{De}$  (blue lines) and the transmission probability  $T$  (red line) are presented in (c), while the light loss  $\eta_{loss}$  by the depolarizing wall is shown in (d). Here, the radius  $r_L$  is 0.8mm (solid lines), 0.6mm (dashed lines), and 0.4mm (dotted lines), respectively.

quency of which is locked to absorption peaks. In this study, we examined the polarization  $P_{ave}^{De}$  at the absorption peaks and the transverse signal  $P_{x,ave}^{De}$  of the SERF magnetometer under various input powers and  $N_2$  pressures.

As  $r_L$  decreases, the effective absorption length increases, and the wall-polarization effect is reduced, leading to a higher polarization  $P_{ave}^{De}$ . However, once the polarization centralized around the illuminating region approaches its maximum value, the total polarization begins to decrease. Meanwhile, reducing the light lost due to wall depolarizing by monotonically decreasing  $r_L$  results in a significant increase in the transmission probability. This increase is particularly noticeable at low  $N_2$  densities (500 Torr in Figs. 9(a) and (b)). For example, with 0.2 mW of input power (dashed lines),  $P_{ave}^{De}$  increases from 0.21 to 0.31 when the beam radius is reduced from  $R$  to  $0.65R$ , while  $T$  increases from 0.007 to 0.06. This one-order increase in transmission probability is advantageous in locking the laser's frequency. Fur-

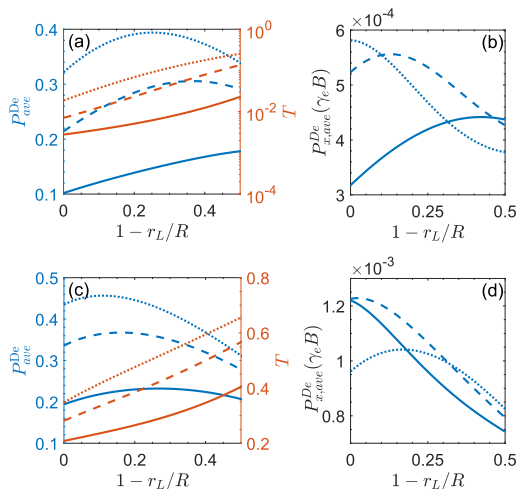


FIG. 9. Average atomic polarization  $P_{ave}^{De}$ , pump laser's transmission probability  $T$ , and transverse signal  $P_{x,ave}^{De}$  of SERF magnetometers at different  $N_2$  pressures and input powers. The  $N_2$  pressures are 500Torr for (a) and (b) and 2000Torr for (c) and (d). The laser input powers are 0.1mW (solid line), 0.2mW (dashes line), and 0.3mW (dotted line), respectively.

thermore, reducing  $r_L$  also results in an increase in the signal  $P_{x,ave}^{De}$ . These characteristics of  $P_{ave}^{De}$ ,  $T$ , and  $P_{x,ave}^{De}$  are consistent across different  $N_2$  densities (2000 Torr in Figs. 9(c) and (d)), although their changes with respect to  $r_L$  are less significant since the wall-depolarizing effect is smaller when more buffer gas is present.

## V. CONCLUSIONS

In this work, we have investigated the wall effect in small atomic vapor cells at high temperatures. By comparing cases with fully depolarizing and nondepolarizing walls, we found that the traditional treatment, which considers only the lowest diffusion mode, underestimates the wall-depolarizing effect in the 2mm-cells. To address this issue, we proposed a theoretical estimation of the ratio between the polarizations for depolarizing and nondepolarizing boundaries.

To demonstrate practical implications of our findings, we focus on the SERF magnetometer and its transverse signal dependence on the wall effect. We derived a theoretical upper-bound for the uncoated cells, which revealed that the optimal signal for cells with depolarizing walls is one order smaller compared to that of nondepolarizing walls. Our study also presents a novel approach to reduce the wall-depolarizing effect by shrinking the beam's radius while keeping its input power, in addition to detuning the pump laser. This method can enhance various physical quantities in concerned, such as the atomic polarization, the transmission probability, and the transverse signal of the SERF magnetometer.

## ACKNOWLEDGMENTS

This work was supported by the National Natural Science Foundation of China Grants No. U2141237 and No.62101070.

### Appendix A: Absorption/Polarization peaks for nondepolarizing walls

In this section, we will prove that the absorption/polarization peaks for nondepolarizing walls are at  $\partial_{\Delta}\mathcal{L}(\Delta) = 0$ .

We first integrate Eq. (2) and acquired

$$I(L) = I(0) e^{-g_I \mathcal{L}(\Delta) \int_0^L dz [1 - P_e(z)]}. \quad (\text{A1})$$

Note that for nondepolarizing cylindrical boundaries,  $I$  and  $P_e$  are uniformly distributed along the radial direction, so they are only functions of  $z$ . Then the derivative of Eq. (A1)  $\partial_{\Delta}I(L)$  reads

$$\begin{aligned} \partial_{\Delta}I(L) &= g_I I(L) [\mathcal{L}(\Delta) \partial_{\Delta} \int_0^L dz P_e(z) - \\ &\int_0^L dz [1 - P_e(z)] \partial_{\Delta}\mathcal{L}(\Delta)]. \end{aligned} \quad (\text{A2})$$

At the peaks,  $\partial_{\Delta}I(L) = 0$  and equivalently  $\partial_{\Delta} \int_0^L dz P_e(z) = 0$  (see Eq. (9) for uniform irradiation case), which consequently gives

$$\int_0^L dz [1 - P_e(z)] \partial_{\Delta}\mathcal{L}(\Delta) = 0. \quad (\text{A3})$$

Since  $1 - P_e(z) > 0$ , the maximal polarization/absorption is at  $\partial_{\Delta}\mathcal{L}(\Delta) = 0$ .

### Appendix B: Estimation of $P_{ave}^{De}/P_{ave}^{NonDe}$ and $\tilde{P}_{x,ave}^{De}$

To acquire an analytical estimation of the ratio  $P_{ave}^{De}/P_{ave}^{NonDe}$ , we first simplify Eq. (1) by assuming the light intensity is unchanged in the vapor cell and neglecting the derivative of the slow-down factor  $q(P_e)$ . Under these approximations, we can express  $P_e^{De}$  for depolarizing boundaries as  $P_e^{De} = f_{xy}(x, y)f_z(z)$ , where its longitudinal dependence is given by:

$$f_z(z) = \frac{\tilde{R}_{op}}{\tilde{R}_{op} + \Gamma_{rel}} \left( 1 - \frac{e^{-z/\lambda_D} + e^{-(L-z)/\lambda_D}}{1 + e^{-L/\lambda_D}} \right), \quad (\text{B1})$$

with  $\tilde{R}_{op} \equiv g_P \mathcal{L}(\Delta) I_0$ . This simplified solution shows that the depolarizing wall only affects a layer with a width of  $\lambda_D$ . Though the solution for the radial direction is more complicated, we can assume that the influence of



the depolarizing wall is similar. Hence, the “unfected” volume can be estimated as

$$\pi (R - \lambda_D)^2 (L - 2\lambda_D). \quad (\text{B2})$$

Up until now, we have assumed an overall constant light intensity,  $I_0$ , in the cell. However, the wall-depolarization length  $\lambda_D$  should be larger because  $I$  decays in both the radial and longitudinal directions. This decay is faster when the light is closer to the walls where the polarization is small, and we can characterize it using the absorption length  $\lambda_L$ . Accounting for this by including a factor of  $\sqrt{1 - \lambda_D/\lambda_L}$  in the ratio  $P_{ave}^{De}/P_{ave}^{NonDe}$ , we obtain

$$\begin{aligned} \frac{P_{ave}^{De}}{P_{ave}^{NonDe}} &\approx \sqrt{1 - \frac{\lambda_D}{\lambda_L}} \frac{\pi (R - \lambda_D)^2 (L - 2\lambda_D)}{\pi R^2 L} \\ &= \sqrt{1 - \frac{\lambda_D}{\lambda_L}} \left(1 - 2\frac{\lambda_D}{L}\right) \left(1 - \frac{\lambda_D}{R}\right)^2. \end{aligned} \quad (\text{B3})$$

For SERF magnetometers, if we ignore the spatial de-

pendence of the light intensity and the atomic polarization, the optimal transverse signal

$$\tilde{P}_x = \frac{\gamma_e B}{2(R_{op} + \Gamma_{rel})},$$

while the  $z$ -direction polarization is  $1/2$ . Taking into account of the wall-depolarizing effect, a factor  $P_{ave}^{De}/P_{ave}^{NonDe}$  is added and the largest transverse signal  $\tilde{P}_{x,ave}^{De}$  for depolarizing walls becomes

$$\tilde{P}_{x,ave}^{De} \approx \max \left[ \frac{P_{ave}^{De}}{P_{ave}^{NonDe}} \frac{\gamma_e B}{2(R_{op}^0 + \Gamma_{rel})} \right]. \quad (\text{B4})$$

However, for large densities of  $N_2$ , Eq. (B4) may overestimate the maximal  $P_{x,ave}^{De}$ . Back to the full expression for the spatial-independent transverse signal

$$P_x = \frac{\gamma_e B R_{op}}{(R_{op} + \Gamma_{rel})^2}, \quad (\text{B5})$$

we obtain Eq. (16).

- 
- [1] I. K. Kominis, T. W. Kornack, J. C. Allred, and M. V. Romalis, *Nature (London)* **422**, 596 (2003).
  - [2] D. Budker, *Nature(London)* **422**, 574 (2003).
  - [3] D. Budker and M. Romalis, *Nat. Phys.* **3**, 227 (2007).
  - [4] W. Happer, E. Miron, S. Schaefer, D. Schreiber, W. A. van Wijngaarden, and X. Zeng, *Phys. Rev. A* **29**, 3092 (1984).
  - [5] T. G. Walker and W. Happer, *Rev. Mod. Phys.* **69**, 629 (1997).
  - [6] S. Appelt, A. B.-A. Baranga, C. J. Erickson, M. V. Romalis, A. R. Young, and W. Happer, *Phys. Rev. A* **58**, 1412 (1998).
  - [7] V. V. Yashchuk, J. Granwehr, D. F. Kimball, S. M. Rochester, A. H. Trabesinger, J. T. Urban, D. Budker, and A. Pines, *Phys. Rev. Lett.* **93**, 160801 (2004).
  - [8] J. Vanier and C. Tamescu, *The quantum physics of atomic frequency standards: recent developments* (CRC Press, 2015).
  - [9] P. Forman, *Science* **249**, 685 (1990).
  - [10] B. Julsgaard, J. Sherson, J. I. Cirac, J. Fiurášek, and E. S. Polzik, *Nature* **432**, 482 (2004).
  - [11] K. Hammerer, A. S. Sørensen, and E. S. Polzik, *Reviews of Modern Physics* **82**, 1041 (2010).
  - [12] C. B. Møller, R. A. Thomas, G. Vasilakis, E. Zeuthen, Y. Tsaturyan, M. Balabas, K. Jensen, A. Schliesser, K. Hammerer, and E. S. Polzik, *Nature* **547**, 191 (2017).
  - [13] N. Fortson, P. Sandars, and S. Barr, *Phys. Today* **56**, 33 (2003).
  - [14] J. M. Amini, C. T. Munger, and H. Gould, *Phys. Rev. A* **75**, 063416 (2007).
  - [15] B. M. Roberts, V. A. Dzuba, and V. V. Flambaum, *Annu. Rev. Nucl. Part. Sci.* **65**, 63 (2015).
  - [16] W. Happer, Y.-Y. Jau, and T. Walker, *Optically Pumped Atoms* (Wiley, New York, 2010).
  - [17] M. Auzinsh, D. Budker, and S. M. Rochester, *Optically polarized atoms* (Physics of Atoms and Molecules (Oxford University Press, New York, 2010), 2010).
  - [18] Z. Wu, *Rev. Mod. Phys.* **93**, 035006 (2021).
  - [19] S. J. Seltzer, *Developments in alkali-metal atomic magnetometry* (Princeton University, 2008).
  - [20] S. Seltzer and M. Romalis, *Journal of Applied Physics* **106**, 114905 (2009).
  - [21] M. E. Wagshul and T. E. Chupp, *Phys. Rev. A* **49**, 3854 (1994).
  - [22] R. Knize, Z. Wu, and W. Happer, in *Advances in atomic and molecular physics*, Vol. 24 (Elsevier, 1988) pp. 223–267.
  - [23] W. Franzen, *Phys. Rev.* **115**, 850 (1959).
  - [24] W. Happer and A. C. Tam, *Phys. Rev. A* **16**, 1877 (1977).
  - [25] J. C. Allred, R. N. Lyman, T. W. Kornack, and M. V. Romalis, *Phys. Rev. Lett.* **89**, 130801 (2002).
  - [26] I. M. Savukov and M. V. Romalis, *Phys. Rev. A* **71**, 023405 (2005).
  - [27] Y. Chang, Y.-H. Guo, and J. Qin, *Phys. Rev. A* **99**, 063411 (2019).
  - [28] A. F. Molisch and B. P. Oehry, *Radiation trapping in atomic vapours* (Oxford University Press, 1998).
  - [29] W. Lee, *Ultra-high Sensitivity Atomic Magnetometers* (Princeton University, 2022).